Tectonophysics 836 (2022) 229414

Contents lists available at ScienceDirect

Tectonophysics

journal homepage: www.elsevier.com/locate/tecto

Slow slip events and flank instability at Mt. Etna volcano (Italy)

Mimmo Palano [a,*], Federica Sparacino [a], Piera Gambino [b], Nicola D'Agostino [c], Stefano Calcaterra [b]

[a] Istituto Nazionale di Geofisica e Vulcanologia, Sezione di Catania, Osservatorio Etneo, Catania 95125, Italy
[b] Italian Institute for Environmental Protection and Research (ISPRA), Rome 00144, Italy
[c] Istituto Nazionale di Geofisica e Vulcanologia, Osservatorio Nazionale Terremoti, Rome 00143, Italy

ARTICLE INFO

Keywords:
Slow slip event
Unstable flank
Distributed slip model
Aseismic deformation
Mt. Etna

ABSTRACT

We analyzed a set of 11 slow slip events occurred during the 2006–2016 period and affecting the GNSS (Global Navigation Satellite System) stations of the unstable flank of Mt. Etna volcano. Observed surface deformation for most of the detected slow slip events, concentrates on the south-eastern edge of the unstable flank while the slow slip events involving the north-eastern edge are less frequent. Such a pattern highlights the existence of two distinct families of events, involving two contiguous sectors of the unstable flank, which occasionally slip together in large slow slip events. The modelled slips also highlight that both contiguous sectors extend ~10–12 km offshore, on areas where active tectonic lineaments such as the ESE (northward of Catania Canyon) and the N102° (along the southern slope of the Riposto Ridge) ones have been recently discovered. Equivalent seismic moments of slow slip events occurred in the last ten years (corresponding to magnitudes in the range 5.4–5.9) are larger than those associated to seismic events observed in the last 200 years, suggesting that most of the deformation affecting the eastern flank occurs aseismically.

1. Introduction

Episodic aseismic slip events are earthquake-like events which, releasing energy over a period of hours to months, have been detected at a variety of tectonic and volcanic environments. These particular events, termed as slow slip events (SSE hereinafter), are becoming increasingly recognized as important, due to their influence on local and regional seismicity. Indeed, recent studies have highlighted that the SSEs occur close to zones of frictional transition from velocity strengthening to velocity weakening (Liu and Rice, 2007; Rubin, 2011; Segall et al., 2010) therefore providing useful information on fault zone properties.

The first detected SSE dates December 1992 and occurred along the San Andreas fault in central California (Linde et al., 1996). This SSE was detected by two borehole strainmeters which were installed closely to the main fault and recorded a transient deformation event of about a week in duration. The rapid increase of continuous GNSS (cGNSS) stations has allowed to detected a large number of SSEs worldwide. The large majority of SSEs has been observed at convergent plate boundaries. Valuable examples come from Cascadia (Dragert et al., 2001, 2004; Brudzinski and Allen, 2007; Haines et al., 2019), New Zealand (Beavan et al., 2007) and Japan (Hirose et al., 1999; Obara and Hirose, 2006; Ito et al., 2013). Sometimes they are associated with seismic tremor (Dragert et al., 2001, 2004; Brudzinski and Allen, 2007; Haines et al., 2019; Beavan et al., 2007), but not exclusively. For example, it has long been recognized that detected SSEs in Cascadia are nearly always accompanied by seismic tremor (Rogers and Dragert, 2003), with a few exceptions for brief times during individual SSEs when slip appears to occur with no obvious tremor (Wech and Bartlow, 2014).

In the last two decades more than 10 SSEs have been identified from cGNSS data at Kilauea volcano southern flank (see Foster et al., 2013 and references therein). These SSEs exhibit surface displacements up to a few centimeters, duration of several hours to 2 days and occur along the offshore portion of the basal decollement (e.g. Montgomery-Brown et al., 2009).

The occurrence of SSEs has been detected also at Mt. Etna from the cGNSS stations covering the continuous seaward moving eastern flank of the volcano (see Palano, 2016 and references therein for additional details). Here, taking into account a new set of cGNSS data acquired at the SiOrNet network (Fig. 1) we improved the results reported in Palano (2016) by extending in time (back and forward) the preexisting SSE catalog. Moreover, we performed a new modelling of the surface deformation associated to each SSE in order to better constrain the slip

* Corresponding author at: Istituto Nazionale di Geofisica e Vulcanologia, Osservatorio Etneo - Sezione di Catania, P.zza Roma 2, I-95123 Catania, Italy
E-mail address: mimmo.palano@ingv.it (M. Palano).

https://doi.org/10.1016/j.tecto.2022.229414
Received 24 January 2022; Received in revised form 13 May 2022; Accepted 14 May 2022
Available online 20 May 2022

distribution pattern on the causative source. Achieved results are discussed in the general setting of the eastern flank of the volcano, in order to provide an improved picture about its complex kinematics and block fragmentation.

2. Mt. Etna background

Mt. Etna is a basaltic Quaternary volcano located on the east coast of Sicily (South Italy) at the front of the Apennine-Maghrebian chain (AMC) (Fig. 1). The volcano developed over the last 500 ka over metamorphic and sedimentary rocks (belonging to the AMC) on its western and northern slopes and over Quaternary plastic clays (accumulated along the Gela-Catania Foredeep at the front of AMC; Branca and Ferrara, 2013). The different geomechanical properties of outcropping rocks coupled with the inhomogeneous long-term updoming (De Guidi et al., 2014) of the volcano have produced a complex basement topography dominated by a 17 km-wide horseshoe-shaped depression beneath the eastern flank (Branca and Ferrara, 2013). Such a complex basement topography gently dips in SE direction and would lead to the large-scale seaward motion of the eastern flank of Mt. Etna as clearly documented since the early 1980s (e.g. Borgia et al., 1992). At the surface, the unstable sector is defined by a 25 km-wide horseshoe-shaped region which encompassing the sedimentary one is bounded by the "NE Rift - Pernicana fault" and by the "South Rift - Mascalucia-Tremestieri - Aci Trezza fault system", respectively on its NE and SE half (Fig. 1). In addition, the presence of compressional structures (e.g. folds) at the toe of the continental margin as well as a prominent ESE lineament with prevailing right-lateral transpressive kinematics, located northward of Catania Canyon has recently been discovered, on the Etnean offshore (Gross et al., 2015; Fig. 1). Furthermore, active tectonics also occurs over the unstable sector and is distributed on a number of shallow faults such as the Timpe (TFS), the Santa Tecla (STF), the Santa Venerina (SVF), the Fiandaca (FF) and the Nizzeti (NF) ones (Fig. 1; Azzaro et al., 2012). The TFS consists of a 20 km long and 5 km wide belt of mainly NNW to N extensional structures with well-developed morphological scarps; the STF and SVF consist of two near parallel faults, which have a NW-SE trend and are characterized by right-lateral slips coupled with minor normal components. The FF is a NW-SE oriented right-lateral fault system with a normal component (Azzaro et al., 2012) which connects southward with the NF system, a set of two NNE to NNW trending faults characterized by linear, up to 100 m high, cumulative scarps (De Guidi et al., 2018).

Geodetic studies (Solaro et al., 2010; Bonforte et al., 2011; Palano, 2016) suggested a complex fragmentation of the unstable flank with the northeastern sector moving faster (up to 61 mm/yr of horizontal and ~15 mm/yr of vertical motion) than the southeastern one (~33 mm/yr and ~2–3 mm/yr for horizontal and vertical motion, respectively). This overall seaward motion is modulated at different spatial and temporal scales by different sources/mechanisms such as vigorous and long lasting inflation/deflation episodes (e.g. Aloisi et al., 2011), episodic or

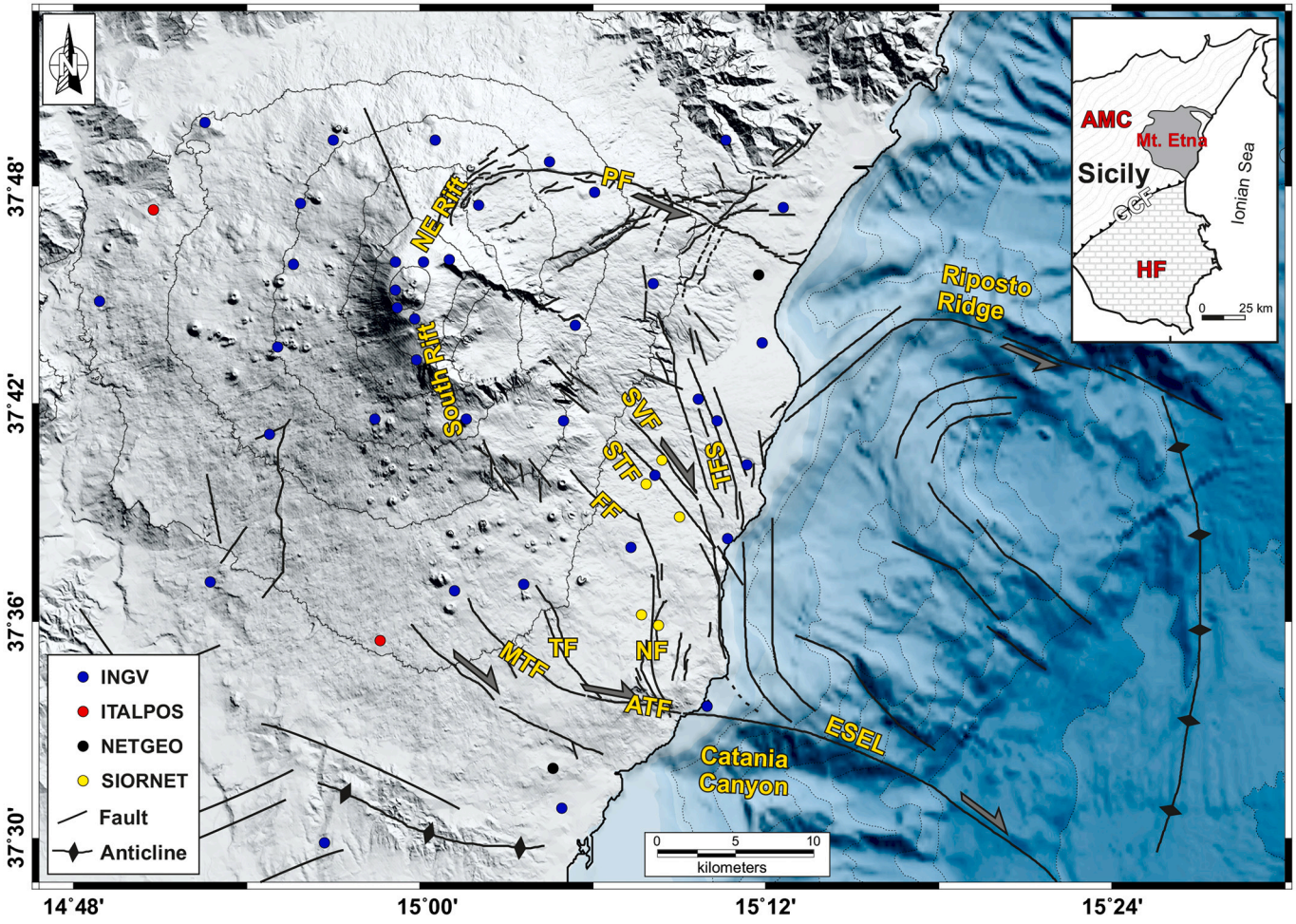

Fig. 1. Simplified tectonic map of Mt. Etna and its eastern offshore. Bathymetry is from www.emodnet-bathymetry.eu. cGNSS stations covering Mt. Etna volcano are reported as colored points. Abbreviations are as follows: PF, Pernicana fault; TFS, Timpe fault system; SVF, Santa Venerina fault; STF, Santa Tecla fault; FF, Fiandaca fault; NF, Nizzeti fault system; TF, Trecastagni fault; MTF, Mascalucia-Tremestieri fault; ATF, Aci Trezza fault; ESEL, ESE lineament. Inset: sketch map of eastern Sicily; AMC, Apennine-Maghrebian chain; HF, Hyblean Foreland; GCF, Gela-Catania Foredeep.

continuous fault creeping (e.g. Palano et al., 2006; Gambino et al., 2011) and large scale post-eruption deformations (e.g. Palano et al., 2009). The definition of the basal sliding surface of Mt. Etna is widely debated and a number of different models have been proposed in the last 3 decades. For instance, Lo Giudice and Rasà (1992) postulate a shallow (~1.5 km) surface with a listric geometry located beneath the volcanic pile of Mt. Etna. Borgia et al. (1992) suggest an approximately 5-km-deep sub-horizontal west-dipping décollement. Tibaldi and Groppelli (2002) suggest the possibility of alternating or contemporaneous movements on both shallow and deep east-dipping slip surfaces under the effects of different source mechanisms. GNSS-based models point to a sliding east-dipping surface located at a depth ranging from 0 to 5 km b.s.l. (see Palano, 2016 and references therein).

3. Data and modelling

3.1. Geodetic data

All available cGNSS data on the eastern flank of Mt. Etna edifice were collected and analyzed in order to take into account the best spatially and temporally station coverage. To this aim we collected data from the following networks:

- Etn@net: this network is managed by the "Osservatorio Etneo" department of "Istituto Nazionale di Geofisica e Vulcanologia". The setting up of this network began in November 2000 reaching a configuration of 13 stations in late summer of 2001 with daily sessions of about 8 h. The network geometry was gradually upgraded over the years in order to cover all the slopes of the volcano edifice and to replace the sites destroyed by natural (lava flows) and human (vandalism) activities or affected by local instability, reaching the current configuration of 33 stations (blue dots in Fig. 1). A continuous acquisition on sessions of 24 h at all the stations was scheduled at least since early 2005. Pillars directly founded on consolidated bedrock represent the largest monument number.
- SiOrNet: this network is currently managed by the Geodetic Group of the Geological Survey of Italy-ISPRA and consists of 5 cGNSS stations installed on some faults segments along the SE slope of Mt. Etna (yellow dots in Fig. 1). The network was established in late 2005 and discontinuously worked until mid-2016. The functioning of the network was restored in late 2018 (Pezzo et al., 2020). Monuments consist on pillars directly founded on consolidated bedrock or steel masts anchored on concrete buildings.
- Italpos: this network is currently managed by Hexagon Geosystems (https://hxgnsmartnet.com/it-it). It was developed to support commercial applications, such as mapping and cadastral purposes and stations are characterized by a wide variety of different monument types. Pillars, or steel masts, anchored to buildings represent the largest number, while monuments directly founded on consolidated bedrock are present in minor percentage. Only 2 stations are installed on the volcano edifice (red dots in Fig. 1); MASC was dismissed on early 2016.
- NetGEO: this network was developed by Geotop (http://www.netgeo.it/) since early 2012. As the Italpos network, NetGEO was developed to support commercial applications. Monuments consist on pillars or steel masts, anchored to buildings. Such a network covers the volcano edifice with 2 stations installed on its eastern flank (black dots in Fig. 1).

All collected data were processed using the GAMIT/GLOBK software (Herring et al., 2018) with IGS precise ephemerides. To improve the overall configuration of the network and tie the regional measurements to an external global reference frame, data coming from 15 continuously operating IGS stations were introduced in the processing. We used the latest absolute receiver antenna models by the IGS and we adopted the Saastamoinen (1972) atmospheric zenith delay models, coupled with the Global Mapping Functions (Böhm et al., 2006) for the neutral atmosphere. Estimated cGNSS daily time series and displacements for specified time intervals were referred to an updated version of the "Etn@ref" reference frame (a local reference frame computed to isolate the Mt. Etna volcanic deformation from the background tectonic pattern; Palano et al., 2010).

From the visual inspection on the daily-based time series, we observed that at stations located along the lower eastern flank (group 1 with red time-series in Fig. 2) each SSE produces or a sudden change (e.g. ELAC and MASC), or a more gradual change with respect to the linear trend of the time-series (e.g. EPOZ). Both changes occur with a finite duration and are characterized by rates that are faster than the long-term seaward motion of the unstable flank. The stations located on the middle sector of the eastern flank (group 2 with blue time-series in Fig. 2), although showing a near continuous eastward motion, are also modulated by deformation related to inflation/deflation magmatic sources. The time-series of all these stations are also locally modulated by episodic creeping of the faults dissecting and/or bordering the unstable flank (see discussion). cGNSS stations externally located with respect the unstable flank (group 3 with time-series colored in black in Fig. 2) are characterized by time series showing no deformation to gentle eastward motion. By inspecting the time-series of ACSA, SCAC, ELAC, MASC and EPOZ (null or very little influenced by the action of the magmatic sources) we detected 11 SSEs with duration grossly ranging from 2 to 67 days (see Fig. 2 and Table 1). On the analyzed time interval, the first SSE occurred in April 2006, while the last one in April 2016, therefore extending in time (back and forward) the SSE catalog previously defined in Palano (2016). Moreover, the time-series of the SiOrNet cGNSS stations allowed also to improve the detection of some SSEs (in term of SSE onset and related duration), leading to some differences with respect to the previous catalog. For each recognized SSE, we determine the amount of displacements by averaging site position in the 3 days preceding and following the event.

3.2. Modelling

The displacement fields were used to constrain isotropic half-space elastic inversion models. Although the faults dissecting and/or bordering the unstable flank might accommodate a fraction of deformation during each SSE, in the following we assumed that the slip occurs only along the basal sliding surface. Indeed, the current density of cGNSS stations on the eastern flank of the volcano doesn't allow to properly differentiate the individual contribute of the basal sliding surface and the other active faults to the total ground deformation field.

The displacement field for SSEs lasting several days could contain a significant contamination from magmatic sources contemporaneously active. In particular, considering the SSEs with duration larger than 10 days, we observed that they occurred during inflation stages of the volcano, for which magmatic source parameters are already available in literature. We therefore subtracted the calculated effects of active magmatic sources from the observed displacement field to obtain the residual field which would correspond to the SSE contribute (see Table 1). Subtracted values range on average from ~3 to 5 mm for the stations located on the upper eastern flank to less than 0.5 mm for stations located along the coastal belt. Estimated residual displacements are reported in Fig. 3.

To determine the spatial distribution of slip for each SSE, we extended up to 36 × 36 km and divided in 15 (along-strike) by 15 (along-dip) squared patches (dimension of 2.4 × 2.4 km) a sliding surface similar to the one inferred in Palano (2016). We also fixed the dip of the sliding surface to 10° (Table 2). We used only the horizontal components of the deformation field being the vertical one too scattered among nearby stations. This choice is motivated by the lack of significant vertical variations related to each SSE on the cGNSS time series. To perform the elastic inversion models for each SSE we used the *GTdef* code (Feng et al., 2012) which finds the optimal model parameters by

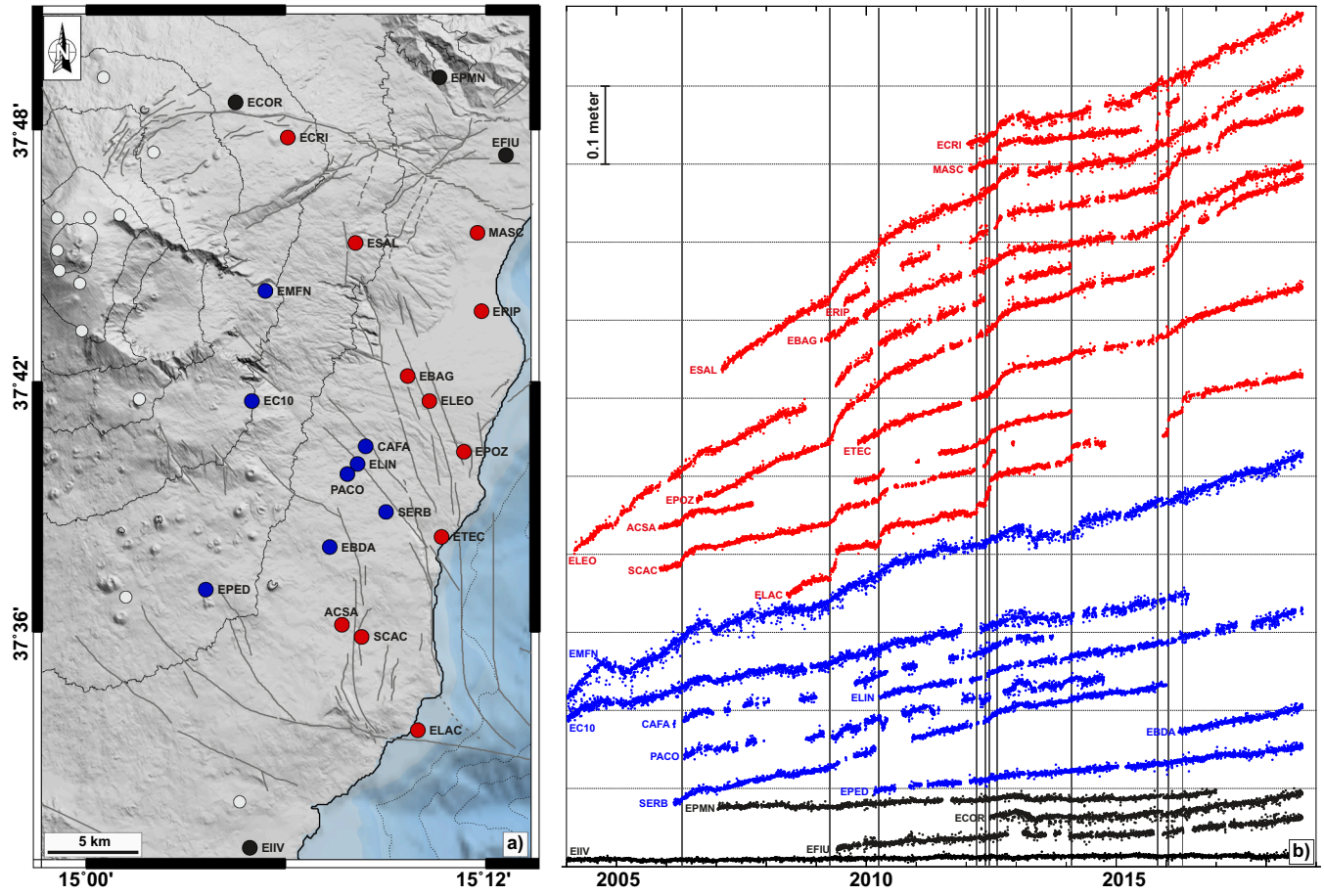

Fig. 2. a) Zoom of the eastern flank of Mt. Etna. The cGNSS stations follow the colour scheme of panel b); stations reported as white points have been not analyzed in this study because largely affected by magma movements along the volcano plumbing system. b) time series of the East component of continuous cGNSS stations installed on the lower and middle eastern flank of Mt. Etna. cGNSS time series are colored according to their main features. cGNSS time series showing sudden change on their linear trend or a change with respect to their long-term trend are colored in red (group 1). cGNSS time series showing a continuous eastward motion, superposed by inflation/deflation deformation are colored in blue (group 2). cGNSS time series showing no deformation to gentle eastward motion and externally located with respect the unstable flank are colored in black (group 3). The vertical dark-gray lines indicate the SSEs occurrence (see Table 1 for details). (For interpretation of the references to colour in this figure legend, the reader is referred to the web version of this article.)

Table 1
Catalog of slow slip events identified in this study. For each SSE, the duration, the geodetic moment (GM) and the estimated magnitude (M_w) are also reported. The deformation related to active magmatic sources has been removed from the displacement field of SSE-01, SSE-02, SSE-03, SSE-05 and SSE-09 by adopting the source parameters available in literature (Pal17, Palano et al., 2017; Alo11, Aloisi et al., 2011; Spa15, Spampinato et al., 2015; Can18, Cannata et al., 2018).

SSE_Id	Event date	Duration (days)	GM (Nm)	M_w	Notes
SSE-01	16/04/2006	13	$1.84{\cdot}10^{17}$	5.48	Pal17
SSE-02	13/04/2009	42	$8.60{\cdot}10^{17}$	5.92	Alo11
SSE-03	27/03/2010	67	$3.86{\cdot}10^{17}$	5.69	Alo11
SSE-04	16/03/2012	5	$2.15{\cdot}10^{17}$	5.52	
SSE-05	15/05/2012	29	$2.42{\cdot}10^{17}$	5.56	Spa15
SSE-06	24/06/2012	4	$1.56{\cdot}10^{17}$	5.43	
SSE-07	10/08/2012	4	$1.49{\cdot}10^{17}$	5.42	
SSE-08	10/02/2014	2	$1.95{\cdot}10^{17}$	5.49	
SSE-09	26/10/2015	12	$2.52{\cdot}10^{17}$	5.57	Can18
SSE-10	14/01/2016	3	$2.45{\cdot}10^{17}$	5.56	
SSE-11	28/04/2016	5	$2.34{\cdot}10^{17}$	5.55	

using a linear least-squares solver scheme. In particular, *GTdef* seeks to solve the linear equation system relating the unknown slips (m) to the observed deformation (d) by applying a two-dimensional second-derivative (Laplacian) operator:

$$\begin{bmatrix} w^{-1}d \\ 0 \end{bmatrix} = \begin{bmatrix} w^{-1}G \\ k^2 D \end{bmatrix} m \quad (1)$$

where w is the diagonal matrix constructed from observation errors, G is the green function matrix, D is the second-order finite difference operator (Jónsson et al., 2002), k^2 controls the weight imposed on the smoothing. The choice of smoothing leads to different model results where increasing smoothing values generally leads to an increase of model misfit. To determine the preferred model for each SSE, a trade-off curve between model misfit and roughness has been computed. The model misfit has been quantified through the chi-square value, while the average second-order finite difference sum of each patch has been used to indicate the model roughness ρ (Jónsson et al., 2002):

$$\rho = \frac{\sum_i |p_i|}{2N} \quad (2)$$

where $p = Dm$ and N is the number of fault patches. The units of ρ are cm/km^2, indicating the average slip gradient (Jónsson et al., 2002). Our preferred models are reported in Fig. 3 and are characterized by k ranging in the 4935–5755 interval (Fig. S1).

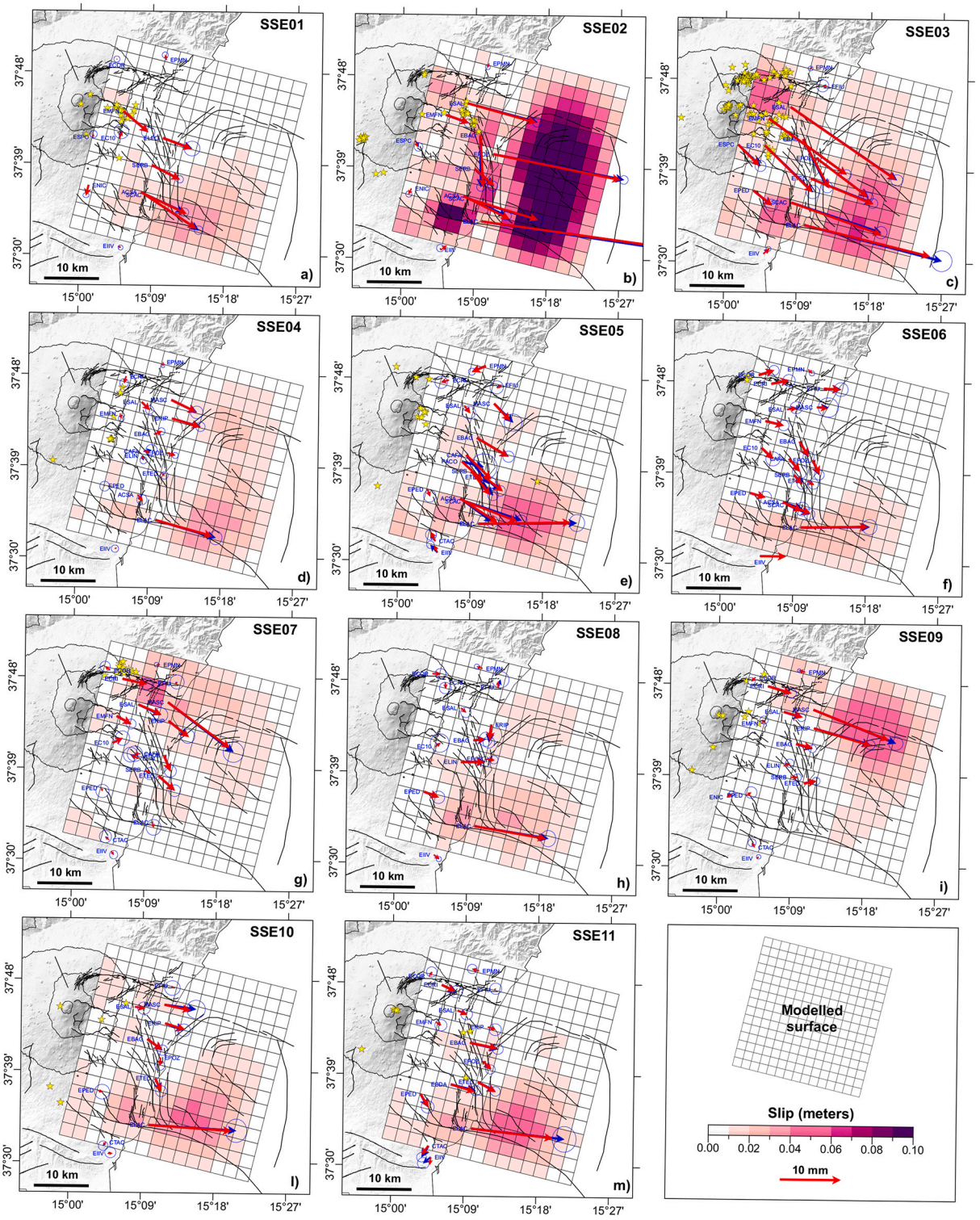

Fig. 3. Observed (blue arrows) and modelled (red arrows) surface displacements related to each detected SSE. Slip distributions on modelled decollement surface are also reported. See Table 1 for additional details. Shallow earthquakes (depth < 5 km) occurred during each SSE are reported as yellow stars (Alparone et al., 2015, 2020a, 2020b, 2022). (For interpretation of the references to colour in this figure legend, the reader is referred to the web version of this article.)

4. Results and discussion

cGNSS stations installed on the lower unstable flank of Mt. Etna showed significant transient displacements (namely slow slip events) in their daily time-series position during a time interval of 10 years, from April 2006 to April 2016 (Fig. 2). By a simple visual inspection of these time-series, we detected 11 SSEs with duration ranging from 2 to 67 days and with a very irregular average recurrence time of 348 ± 361 days (Table 1). As above mentioned, we extended in time (back and forward) the SSE catalog previously defined in Palano (2016), with some improvements on the definition of SSEs starting and temporal length, thank also to the inedited cGNSS stations of the SiOrNet network, installed on

Table 2
Parameters of the modelled sliding surface. The position (latitude, longitude and depth) indicates the top-center of the modelled surface. Depth (positive downward) is referred to the mean elevation of cGNSS stations used in this study, namely 1100 m above sea level.

Longitude (°)	15.03
Latitude (°)	37.70
Depth (m)	500
Length (km)	36.0
Width (km)	36.0
Azimuth (°)	13.5
Dip (°)	10.0

the SE edge of the unstable flank. In particular, these last stations show time-series where any change with respect to the linear trend is easily detectable (Fig. 2b), because of their proximity to the SSE sources. With respect to the previous catalog, changes are related to the starting and the temporal length of SSE-02, SSE-03, SSE-05 and SSE-07 (Table 1).

4.1. Surface deformation and modelled slip distribution

For each detected SSE, we estimated the surface deformation field which, in a successive step, was modelled to infer the spatial distribution of slip on a shallow sliding surface. Observed surface deformation (Fig. 3) for most of the detected SSEs, mainly concentrates on the south-eastern edge of the onshore unstable sector of the volcano edifice. Such a features is well evident for SSE-01, SSE-03, SSE-04, SSE-05, SSE-06, SSE-08, SSE-10 and SSE-11 (Fig. 3), while SSEs involving the north-eastern edge are less frequent (SSE-07 and SSE-09). Therefore, the overall SSEs sequence highlights the existence of two distinct families of events involving the two contiguous sectors of the sliding flank as already suggested by Palano (2016), which occasionally slip together in large SSEs as observed during SSE-02. Moreover, the SiOrNet cGNSS stations allow to add new constrains to the deformation mode of the southern part of unstable flank of Mt. Etna. A primary key-feature is the differential motion observed along the Nizzeti faults, well captured by ACSA and SCAC stations (Figs. 2 and 3) and resulting in a general E-W extensional deformation. This feature is evident only in early SSEs since ACSA and SCAC worked until early 2014 and mid-2012, respectively. However, extensional deformation has been also observed by episodic measurements carried out along this sector of the volcano during November 2014–April 2017 (De Guidi et al., 2018), highlighting a significant role of the Nizzeti faults in controlling both the long- and the short-term patterns of deformation. A similar behavior has been also observed for the Timpe faults with a general eastward increase of displacements (Palano, 2016). Some shallow seismic swarms occurred during SSE-01, SSE-02, SSE-03, SSE-05 and SSE-07 (Fig. 3a,b,c,e,g), however the cumulative magnitude of the events (generally <3.6, with the exception of the M4.3 2010 earthquake striking the Pernicana fault;

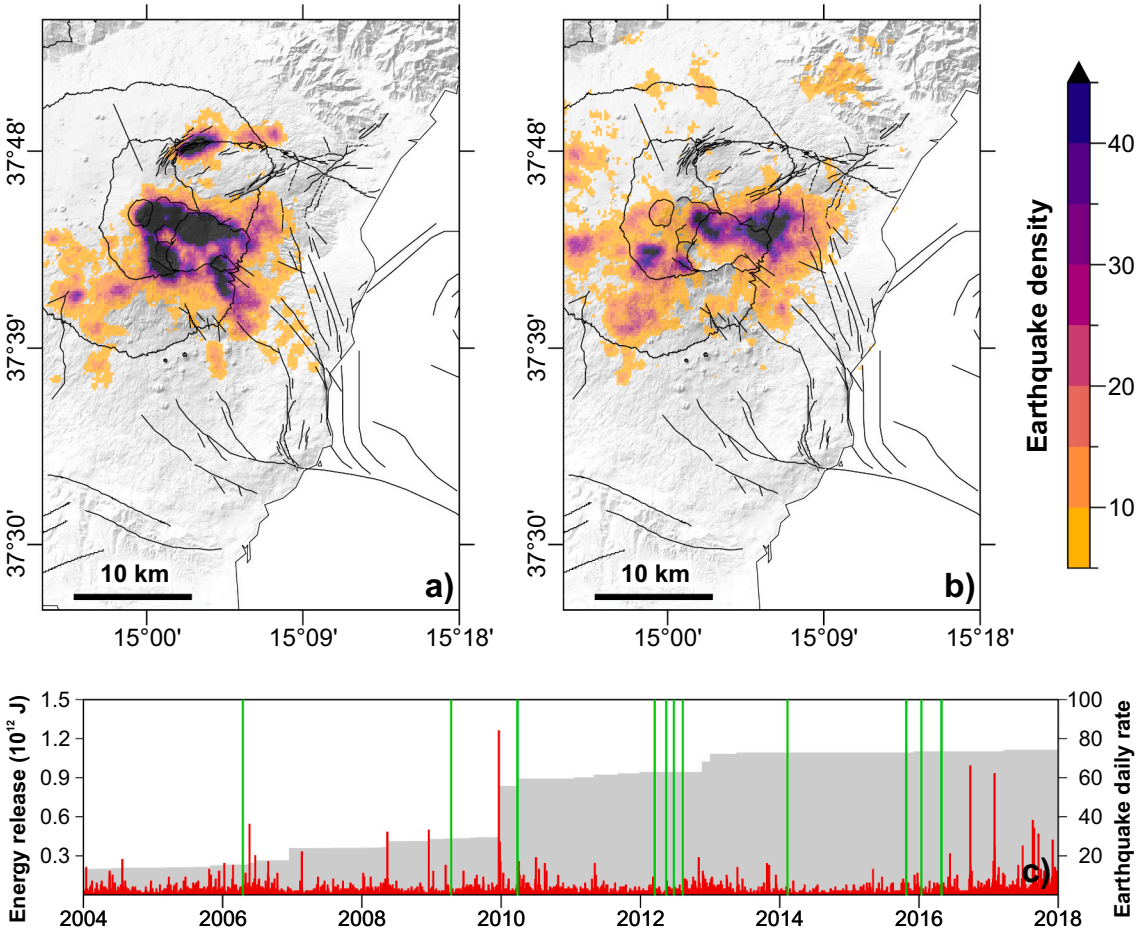

Fig. 4. Density distribution for a) shallow (depth < 5 km) and b) deep (depth < 5 km) earthquakes occurred during the January 2004–December 2017 period. The study area was sampled in 0.002° longitude x 0.002° latitude and colors indicate the number of events within each cell. c) Daily earthquake occurrence (red bars) and related cumulated energy release (gray bars) from January 2004 to December 2017. The vertical green lines indicate the SSEs occurrence (see Table 1). The used catalogs are from Alparone et al. (2015, 2020a, 2020b, 2022). (For interpretation of the references to colour in this figure legend, the reader is referred to the web version of this article.)

Guglielmino et al., 2011) are too small to fully account for the displacements observed during the related SSE. These earthquakes are not associated with the area affected by largest displacements and generally occurred after the SSE onset, therefore suggesting their nucleation as a passive response of faults bordering (SSE-03 and SSE-07; Fig. 3c,g) and dissecting (SSE-01 and SSE-02; Fig. 3a,b) the unstable sector during its sudden ESE-ward motion. Shallow seismicity (depth < 5 km) occurred during the 2004–2017 period is mainly located beneath the central-western portion of the eastern flank, defining a large seismogenic volume (Fig. 4a). A small seismogenic volume can be recognized along the western and central sectors of the Pernicana (Fig. 4a). Deep seismicity (depth > 5 km) shows a spatial pattern similar to the shallow one, involving however also a volume located between the summit area and the mid-southern flank of the volcano (Fig. 4b). Seismicity beneath the lower eastern flank is scant and no significant change in terms of daily number of earthquakes and/or seismic release can be related to the SSEs occurrence (Fig. 4c).

Some cGNSS stations located along the coastal belt (ELAC, MASC and ERIP) are characterized by large displacements, suggesting a causative source located in the closest offshore region. Conversely, EPOZ and ETEC stations showed small to moderate displacements during each SSE, which is comparable in magnitude with the ones measured at stations located in the middle eastern flank. This aspect suggests that the magnitude of deformation is not controlled only by the "station-source" distance, but requires an additional external control. Since along the coastal belt, the sedimentary basement is located at very shallow depth (Branca and Ferrara, 2013), we evaluate a possible correlation between "displacement" and "volcanic cover thickness". To this aim, for each SSE, we estimated both the daily displacement (i.e. the ratio between the total displacement and the event duration) and the volcanic cover thickness (by subtracting the sedimentary basement surface from the TINITALY digital elevation model; Fig. 5a; Tarquini et al., 2007). Both estimated parameters are reported in Fig. 5b: at a first glance, the average daily slip (s) is inversely correlated with the volcanic cover thickness (v) and could be described as:

$$s = -0.256 log(v) + 1.964 \quad (3)$$

In particular, the average daily slip of ELAC, MASC and ERIP stations appears influenced by the thin volcanic cover (less than 5–10 m), while on the other stations the volcanic cover thickness doesn't significantly affect the daily slip during each SSEs. Therefore, the pattern of deformation along the coastal area seems to be related to the volcanic cover thickness: thinner the volcanic cover is, larger the displacement rate will be. Although heterogeneous rheological properties within the sedimentary basement or within the volcanic cover, and/or strain decoupling between surface brittle ruptures and plastic deformation in the underlying clay basement could be invoked to explain such a correlation, its physical significance remains unclear and requires additional studies and more data to be properly quantified and understood. The establishment of new cGNSS stations along the coastal area, especially on these sectors characterized by thin volcanic cover would represent a good starting point for these future studies.

The finer model resolution as well as the large size of the planar source used in this study allowed to get a slip distribution on the basal sliding surface much better that the one achieved in Palano (2016), where the slip was not properly constrained at the edges of the adopted source because of its small size. Looking at the new results, for SSEs occurring more frequently, the slip distribution concentrates with values up to 6 cm on the southeastern sector of the sliding surface, ~10 km offshore in correspondence of the prominent ESE lineament (Fig. 3) discovered by (Chiocci et al., 2011). Such a sector also includes the segment of the ESE lineament where an 8-day-long SSE occurred in May 2017, as observed by seafloor geodetic data (Urlaub et al., 2018). Regarding the SSEs involving the north-eastern edge of the unstable flank, the slip distribution on the modelled surface concentrates ~12 km offshore beneath the Riposto Ridge (Fig. 3), a structural high related to

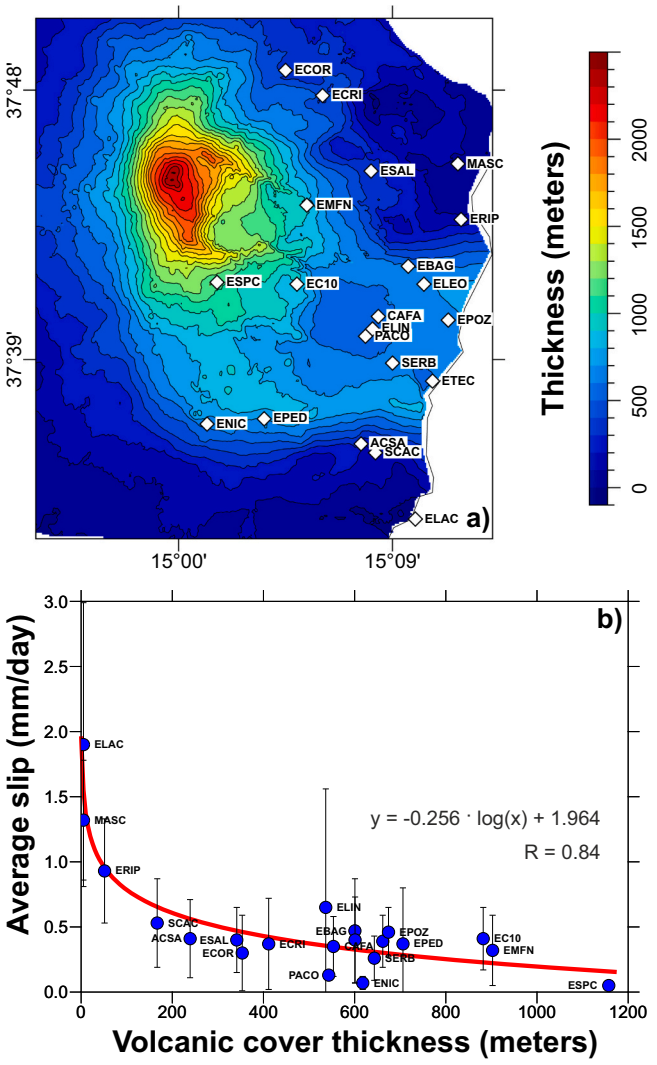

Fig. 5. a) Estimated volcanic cover thickness computed as the height difference between the TINITALY digital elevation model (Tarquini et al., 2007) and the sedimentary basement surface (Branca and Ferrara, 2013). b) Correlation between volcanic cover thickness and daily displacement (see text for details).

the Apennine thrust belt (Chiocci et al., 2011). The southern slope of the Riposto Ridge is marked by a ~ 16-km-long tectonic lineament mapped from ~6 km from the coast up to the flat-floor depression at the toe of the continental margin with a N102° attitude (Fig. 1; Chiocci et al., 2011). This lineament would represent the offshore prolongation of the most active splay of the Pernicana fault, however the lack of clear morphological evidences, doesn't support such a direct connection (Chiocci et al., 2011; Gross et al., 2015; Urlaub et al., 2022). It must be noted, however, that the seaward motion measured on-land, on the northeastern edge of the unstable flank, needs to be adsorbed on offshore structures. Since the seismic data reported in Chiocci et al. (2011), Gross et al. (2015) and Urlaub et al. (2022) also doesn't show clear evidences of contractional structures in the near offshore, where the most active onshore splay of the Pernicana fault intersects the coast, it is more realistic that the motion is transferred/adsorbed to the east, by the N102° lineament or by a not yet discovered sub-parallel fault.

The slip distribution allows us to estimate the geodetic magnitude of each SSE (Table 1); by assuming a rigidity value of 15 GPa, estimated magnitude range between 5.4 (SSE-07) and 5.9 (SSE-01). Such a magnitude range is generally larger than the maximum magnitude (~5.2) estimated for earthquakes occurring at Mt. Etna in the last 200 years (Azzaro et al., 2015), therefore confirming the prevalent aseismic

deformation of the unstable flank (Rasà et al., 1996).

4.2. General considerations and implications

Previous InSAR-based studies (Solaro et al., 2010; Bonforte et al., 2011) defined geometry and kinematics of some blocks dissecting the unstable flank of the volcano, however a set of different deformation patterns observed in the last two decades depicts a complex block fragmentation of this flank, where, beside the slow slip events analyzed in this study, other different sources/mechanisms contributed at different spatial and temporal scales to its continuous seaward motion:

- The onset of energetic volcanic events such as the October 2002–January 2003 eruption (Andronico et al., 2005) and the 24 December 2018 dyke intrusion (Pezzo et al., 2020) activated some hidden and blind fault segments, well highlighting the mentioned above complexity. For instance, the 2002–2003 eruption was accompanied by significant ground deformation of the eastern flank mainly concentrated on its northern half, along the Pernicana fault and the Santa Tecla, Santa Venerina and Timpe faults, where few energetic seismic events (magnitude up to 4.4) also occurred (Neri et al., 2005). Conversely, the 24 December 2018 dyke intrusion led to extensive deformation of the eastern flank coupled with the occurrence of a shallow M4.9 earthquake on 26 December 2018 striking the Fiandaca fault on the southern sector of the unstable flank (Pezzo et al., 2020).
- Significant post-eruption deformations of the unstable flank, have been also documented for ~6 months after the 2002–2003 (Palano et al., 2009) and 2018 (Pezzo et al., 2020) eruption onsets.
- Co-seismic displacements along the Pernicana fault related to M > 3.5 earthquakes which generally produce large surface fractures and damage to man-made features (e.g. Azzaro et al., 1998; Bonforte et al., 2007; Guglielmino et al., 2011).
- Episodic or continuous creeping of the faults dissecting and/or bordering the unstable flank (Rasà et al., 1996; Palano et al., 2006; Gambino et al., 2011).
- Vigorous and long lasting inflation/deflation episodes of the volcano edifice generally produce a pattern of deformation exponentially decreasing with the increase of distance from the magmatic source (Lisowski, 2007): this results in a significant deformation at the stations located at upper and middle elevations, and a very small motion at stations located along the coast (e.g. Aloisi et al., 2011; Bruno et al., 2012; Spampinato et al., 2015).

The temporal modulation of these sources/mechanisms led to substantial changes of the displacement rates on the unstable flank. For instance, horizontal rates from ~33 mm/yr to ~61 mm/yr have been estimated for the 2003–2015 period for the southeastern and northern boundary of the sliding flank, respectively (Palano, 2016). Horizontal rates of ~28 mm/yr have been geodetically estimated during the 1997–2001 period (Palano et al., 2006) along the Pernicana fault, which are slight larger than the values estimated historically (Azzaro et al., 1998) and about an order of magnitude higher than the slip-rate estimated from geologic marker offsets (Azzaro et al., 2012). Geodetic vertical rates estimated for the 2003–2015 period depict a general subsidence with rates of ~15 mm/yr along the Pernicana fault, and of ~2–3 mm/yr along the faults bordering the southern boundary of the unstable flank (Palano, 2016). Such a general subsidence, although occurring at very low rates, can be also inferred by taking into account the available geologic estimations (Azzaro et al., 2012). These observations highlight that the highest deformation rates occur along the northern part of the unstable sector and are spatially and temporally modulated by the sources mentioned above, with the occurrence of frequent small-to-moderate shallow earthquakes on its western side, and sporadic short-term SSEs on its the eastern side. The southern part deforms at rates generally half the ones measured on the northern part and most of the detected SSEs concentrates on its southeastern edge. Moreover, the detection of a SSE occurred in May 2017 on the offshore ESE lineament (Urlaub et al., 2018), whose associated deformation was however not observed at the nearest inland cGNSS station (ELAC; Fig. 2), suggest that SSEs might occurs also on the offshore sector of the unstable flank and would be characterized by limited spatial extent. All these observations clearly evidence a complex block fragmentation of the unstable flank of Mt. Etna where the flank-scale seaward motion is significantly partitioned among the steep creeping/seismogenic faults bordering the blocks.

Our approach to model the surface deformation field of the unstable flank of Mt. Etna provides a good fit of the observed deformation, assuming however that it is entirely associated to slip along the basal sliding surface. Additional sources such as the faults bordering the unstable sector and the blocks inside it have been not considered in our approach, despite their proved role on accommodating/modulating a fraction of the observed deformation. Another limitation of our approach is that it models only static deformation patterns, while as mentioned above a number of sources/mechanisms contributes over different time spans to the observed deformation. Therefore, to properly constrain and quantify all the active sources modulating the seaward motion of the unstable flank of the volcano, a time-dependent modelling approach would represent an interesting topic for future studies. A densification of the current cGNSS network, especially across the active faults of the unstable flank as well as along the coastal area will greatly improve the observational dataset leading to more robust model set-up and on turn, to a better definition of the active sources of deformation. In addition, the use of techniques aimed to the displacement patterns match as the one proposed in Montgomery-Brown et al. (2009) will improve the detection of small events that may be close to the noise level in the cGNSS time series. The use of complementary cGNSS and InSAR observations will furnish high precision measurements of ground deformation with extensive coverage for most of the eastern flank of the volcano, therefore providing robust datasets to explore complex deformation models as recently performed by Camacho et al. (2020). Furthermore, the use of continuous seafloor geodetic dataset could furnish additional information on offshore structures and their associated kinematics, as well as to properly decipher the onshore/offshore extent of deformation signature of SSEs, providing therefore relevant constrain to models set-up. The joined use of both on- and offshore datasets would represent a substantial onward step for future studies at Mt. Etna as well as other active volcanoes.

The seaward motion of the unstable flank would pose a potential threat to the whole region since large submarine landslides, or subaerial landslides plunging into the sea, could trigger tsunamis which on turn can hit the densely populated coasts surrounding the eastern Mediterranean Sea. A large tsunami hitting the eastern Mediterranean in early Holocene has been correlated with the collapse of the Valle del Bove (Pareschi et al., 2006), however such a correlation is highly debated (Vigliotti, 2008). Besides this event, no other tsunamis have been triggered by volcanic and/or flank collapse episodes at Mt. Etna volcano, at least since 6150 BCE (Maramai et al., 2021), therefore highlighting their very rare occurrence. This is not surprising and indeed, the occurrence of a large landslide at Mt. Etna, at least in the near future, is highly improbable because of the low slope of the volcano edifice (~10° on average) and the slow (~61 mm/yr) seaward motion of the unstable flank. The triggering of tsunamis by large SSEs can be excluded too because of the low daily displacement rates (~2 mm/day) currently observed for each SSE from the cGNSS stations (Fig. 4).

5. Conclusive remarks

By inspecting the daily time series of the cGNSS stations located on the unstable flank of Mt. Etna we detected 11 SSEs occurred during the April 2006–April 2016 time interval.

Achieved results provide new hints on the flank instability process

affecting Mt. Etna and would be useful to study possible differences and/or similarities at other spreading volcanoes.

Main conclusions can be summarized as following:

- Observed surface deformation for most of the detected SSEs, concentrates on the south-eastern edge of the unstable flank while SSEs involving the north-eastern edge are less frequent.
- The overall SSEs sequence highlights the existence of two distinct families of events involving the two contiguous sectors of the sliding flank, which occasionally slip together in large SSEs.
- The modelled slips put in evidence that both contiguous sectors extend ~10–12 km offshore, on areas where tectonic lineaments such as the ESE (northward of Catania Canyon) and the N102° (along the southern slope of the Riposto Ridge) ones have been discovered in the last two decades.
- The faults dissecting the unstable flank control both the long- and the short-term patterns of seismic and aseismic deformation.
- The magnitude values of the SSEs sequence range in the 5.4–5.9 interval; these values are larger than the maximum observed one (at least in the last 200 years), evidencing as most of the deformation affecting the eastern flank occurs in aseismic mode.

CRediT authorship contribution statement

Mimmo Palano: Conceptualization, Methodology, Resources, Software, Formal analysis, Data curation, Validation, Writing – review & editing. **Federica Sparacino:** Methodology, Resources, Software, Formal analysis, Validation, Writing – review & editing. **Piera Gambino:** Resources, Formal analysis, Investigation, Data curation, Validation, Writing – review & editing. **Nicola D'Agostino:** Methodology, Resources, Formal analysis, Investigation, Validation, Writing – review & editing. **Stefano Calcaterra:** Resources, Formal analysis, Investigation, Data curation, Validation, Writing – review & editing.

Declaration of Competing Interest

All the authors know and concur with the submission of this manuscript to **Tectonophysics** journal and declare no conflict of interests.

Acknowledgements

We thank Morelia Urlaub and an anonymous reviewer for their constructive comments that helped improving the manuscript. The Editor (Claire A. Currie) is acknowledged for the efficient editorial management. We thank also Daniele Pellegrino and Mario Pulvirenti who ensure the maintenance and acquisition of GNSS data. We are grateful to Andrew V. Newman and his research group for sharing the *GTdef* code used in this study. The figures were made using the Generic Mapping Tools v6.0.0 software (Wessel et al., 2019). The cGNSS data used in this study have been processed in the framework of the Project "Paroxysmal volcanic events and seaward motion at Mt. Etna: an improved picture from a geodetic and seismological perspective" (Progetti di Ricerca Libera) funded by INGV.

Appendix A. Supplementary data

Supplementary data to this article can be found online at https://doi.org/10.1016/j.tecto.2022.229414.

References

Alparone, S., Maiolino, V., Mostaccio, A., Scaltrito, A., Ursino, A., Barberi, G., D'Amico, S., Di Grazia, G., Giampiccolo, E., Musumeci, C., Scarfì, L., Zuccarello, L., 2015. Mt. Etna Seismic Catalog 2000–2010 [Data set]. Istituto Nazionale di Geofisica e Vulcanologia (INGV) - Osservatorio Etneo. https://doi.org/10.13127/etnasc/2000_2010.

Alparone, S., Barberi, G., Di Grazia, G., Giampiccolo, E., Maiolino, V., Mostaccio, A., Musumeci, C., Scaltrito, A., Ursino, A., 2020a. Mt. Etna Seismic Catalog 2011–2013 (Version 1) [Data set]. Istituto Nazionale di Geofisica e Vulcanologia (INGV). https://doi.org/10.13127/ETNASC/2011_2013.

Aloisi, M., Mattia, M., Ferlito, C., Palano, M., Bruno, V., Cannavò, F., 2011. Imaging the multi-level magma reservoir at Mt. Etna volcano (Italy). Geophys. Res. Lett. 38 (16), L16306. https://doi.org/10.1029/2011gl048488.

Alparone, S., Barberi, G., Di Grazia, G., Giampiccolo, E., Maiolino, V., Mostaccio, A., Musumeci, C., Scaltrito, A., Tuvè, T., Ursino, A., 2020b. Mt. Etna Seismic Catalog 2014–2016 (Version 1) [Data set]. Istituto Nazionale di Geofisica e Vulcanologia (INGV). https://doi.org/10.13127/ETNASC/2014_2016.

Alparone, S., Barberi, G., Di Grazia, G., Giampiccolo, E., Maiolino, V., Mostaccio, A., Musumeci, C., Scaltrito, A., Tuvè, T., Ursino, A., 2022. Mt. Etna Seismic Catalog 2017–2019 (Version 1) [Data set]. Istituto Nazionale di Geofisica e Vulcanologia (INGV). https://doi.org/10.13127/ETNASC/2017_2019.

Andronico, D., Branca, S., Calvari, S., Burton, M., Caltabiano, T., Corsaro, R.A., Del Carlo, P., Garfì, G., Lodato, L., Miraglia, L., Murè, F., Neri, M., Pecora, E., Pompilio, M., Salerno, G., Spampinato, L., 2005. A multi-disciplinary study of the 2002-03 Etna eruption: insights into a complex plumbing system. Bull. Volcanol. 67, 314–330. https://doi.org/10.1007/s00445-004-0372-8.

Azzaro, R., Ferreli, L., Michetti, A.M., Serva, L., Vittori, E., 1998. Environmental hazard of capable faults: the case of the Pernicana Fault (Mt. Etna, Sicily). Nat. Hazards 17 (2), 147–162. https://doi.org/10.1023/A:1008034422086.

Azzaro, R., Branca, S., Gwinner, K., Coltelli, M., 2012. The volcano-tectonic map of Etna volcano, 1:100.000 scale: morphotectonic analysis from high-resolution DEM integrated with geologic, active faulting and seismotectonic data. It. J. Geosci. (Boll. Soc. Geol. It.) 131 (1), 153–170. https://doi.org/10.3301/IJG.2011.29.

Azzaro, R., D'Amico, S., Tuvè, T., 2015. Seismic hazard assessment in the volcanic region of Mt. Etna (Italy): a probabilistic approach based on macroseismic data applied to volcano-tectonic seismicity. Bull. Earthq. Eng. 14 (7), 1813–1825. https://doi.org/10.1007/s10518-015-9806-2.

Beavan, J., Wallace, L., Fletcher, H., Douglas, A., 2007. Slow Slip events on the Hikurangi Subduction Interface, New Zealand. In: Tregoning, P., Rizos, C. (Eds.), Dynamic Planet. International Association of Geodesy Symposia, vol. 130. Springer, Berlin, Heidelberg, pp. 438–444. https://doi.org/10.1007/978-3-540-49350-1_64.

Böhm, J., Niell, A., Tregoning, P., Schuh, H., 2006. Global Mapping Function (GMF): a new empirical mapping function based on numerical weather model data. Geophys. Res. Lett. 33 (7), L07304 https://doi.org/10.1029/2005GL025546.

Bonforte, A., Gambino, S., Guglielmino, F., Obrizzo, F., Palano, M., Puglisi, G., 2007. Ground deformation modeling of flank dynamics prior to the 2002 eruption of Mt. Etna. Bull. Volcanol. 69 (7), 757–768. https://doi.org/10.1007/s00445-006-0106-1.

Bonforte, A., Guglielmino, F., Coltelli, M., Ferretti, A., Puglisi, G., 2011. Structural assessment of Mount Etna volcano from Permanent Scatterers analysis. Geochem. Geophys. Geosyst. 12 (2), Q02002 https://doi.org/10.1029/2010GC003213.

Borgia, A., Ferrari, L., Pasquarè, G., 1992. Importance of gravitational spreading in the tectonic and volcanic evolution of Mount Etna. Nature 357 (6375), 231–235. https://doi.org/10.1038/357231a0.

Branca, S., Ferrara, V., 2013. The morphostructural setting of Mount Etna sedimentary basement (Italy): Implications for the geometry and volume of the volcano and its flank instability. Tectonophysics 586, 46–64. https://doi.org/10.1016/j.tecto.2012.11.011.

Brudzinski, M.R., Allen, R.M., 2007. Segmentation in episodic tremor and slip all along Cascadia. Geology 35 (10), 907–910. https://doi.org/10.1130/G23740A.1.

Bruno, V., Mattia, M., Aloisi, M., Palano, M., Cannavò, F., Holt, W.E., 2012. Ground deformations and volcanic processes as imaged by CGPS data at Mt. Etna (Italy) between 2003 and 2008. J. Geophys. Res. Solid Earth 117 (B7), B07208. https://doi.org/10.1029/2011JB009114.

Camacho, A.G., Fernández, J., Samsonov, S.V., Tiampo, K.F., Palano, M., 2020. Multisource 3D modelling of elastic volcanic ground deformations. Earth Planet. Sci. Lett. 547, 116445 https://doi.org/10.1016/j.epsl.2020.116445.

Cannata, A., Di Grazia, G., Giuffrida, M., Gresta, S., Palano, M., Sciotto, M., Viccaro, M., 2018. Space-Time evolution of magma storage and transfer at Mt. Etna volcano (Italy): the 2015-2016 re-awakening of voragine crater. Geochem. Geophys. Geosyst. 19, 471–495. https://doi.org/10.1002/2017GC007296.

Chiocci, F.L., Coltelli, M., Bosman, A., Cavallaro, D., 2011. Continental margin large-scale instability controlling the flank sliding of Etna volcano. Earth Planet. Sci. Lett. 305 (1–2), 57–64. https://doi.org/10.1016/j.epsl.2011.02.040.

De Guidi, G., Imposa, S., Scudero, S., Palano, M., 2014. New evidence for Late Quaternary deformation of the substratum of Mt. Etna volcano (Sicily, Italy): clues indicate active crustal doming. Bull. Volcanol. 76, 816. https://doi.org/10.1007/s00445-014-0816-8.

De Guidi, G., Brighenti, F., Carnemolla, F., Imposa, S., Marchese, S.A., Palano, M., Scudero, S., Vecchio, A., 2018. The unstable eastern flank of Mt. Etna volcano (Italy): first results of a GNSS-based network at its southeastern edge. J. Volcanol. Geotherm. Res. 357, 418–424. https://doi.org/10.1016/j.jvolgeores.2018.04.027.

Dragert, H., Wang, K., James, T.S., 2001. A silent slip event on the deeper Cascadia subduction interface. Science 292 (5521), 1525–1528. https://doi.org/10.1126/science.1060152.

Dragert, H., Wang, K., Rogers, G., 2004. Geodetic and seismic signatures of episodic tremor and slip in the northern Cascadia subduction zone. Earth Planet. Space 56 (12), 1143–1150. https://doi.org/10.1186/BF03353333.

Feng, L., Newman, A.V., Protti, M., González, V., Jiang, Y., Dixon, T.H., 2012. Active Deformation near the Nicoya Peninsula, Northwestern Costa Rica, between 1996 and 2010: Interseismic Megathrust Coupling. J. Geophys. Res. 117, B06407. https://doi.org/10.1029/2012JB009230.

Foster, J.H., Lowry, A.R., Brooks, B.A., 2013. Fault frictional parameters and material properties revealed by slow slip events at Kilauea volcano, Hawaii. Geophys. Res. Lett. 40, 6059–6063. https://doi.org/10.1002/2013GL058234.

Gambino, S., Bonforte, A., Carnazzo, A., Falzone, G., Ferrari, F., Ferro, A., Guglielmino, F., Laudani, G., Maiolino, V., Puglisi, G., 2011. Displacement across the Trecastagni Fault (Mt. Etna) and induced seismicity: the October 2009 to January 2010 episode. Ann. Geophys. 54 (4), 414–423. https://doi.org/10.4401/ag-4841.

Gross, F., Krastel, S., Geersen, J., Behrmann, J.H., Ridente, D., Chiocci, F.L., Bialas, J., Papenberg, C., Cuzur, D., Urlaub, M., Micallef, A., 2015. The limits of seaward spreading and slope instability at the continental margin offshore Mt Etna, imaged by high resolution 2D seismic data. Tectonophysics 667, 63–76. https://doi.org/10.1016/j.tecto.2015.11.011.

Guglielmino, F., Bignami, C., Bonforte, A., Briole, P., Obrizzo, F., Puglisi, G., Stramondo, S., Wegmüller, U., 2011. Analysis of satellite and in situ ground deformation data integrated by the SISTEM approach: the April 3, 2010 earthquake along the Pernicana fault (Mt. Etna-Italy) case study. Earth Planet. Sci. Lett. 312 (3–4), 327–336. https://doi.org/10.1016/j.epsl.2011.10.028.

Haines, J., Wallace, L.M., Dimitrova, L., 2019. Slow slip event detection in Cascadia using vertical derivatives of horizontal stress rates. J. Geophys. Res. Solid Earth 124 (5), 5153–5173. https://doi.org/10.1029/2018JB016898.

Herring, T.A., King, R., Floyd, M.A., McClusky, S.C., 2018. Introduction to GAMIT/GLOBK, Release 10.7. Massachusetts Institute of Technology, Cambridge, UK. https://www-gpsg.mit.edu.

Hirose, H., Hirahara, K., Kimata, F., Fujii, N., Miyazaki, S., 1999. A slow thrust slip event following the two 1996 Hyuganada earthquakes beneath the Bungo Channel, southwest Japan. Geophys. Res. Lett. 26 (21), 3237–3240. https://doi.org/10.1029/1999GL010999.

Ito, Y., Hino, R., Kido, M., Osada, Y., Inazu, D., Ohta, Y., Inuma, T., Ohzono, M., Mishina, M., Suzuki, K., Tsuji, T., Ahi, J., 2013. Episodic slow slip events in the Japan subduction zone before the 2011 Tohoku-Oki earthquake. Tectonophysics 600, 14–26. https://doi.org/10.1016/j.tecto.2012.08.022.

Jónsson, S., Zebker, H., Segall, P., Amelung, F., 2002. Fault slip distribution of the 1999 Mw 7.1 Hector Mine, California, earthquake, estimated from satellite radar and GPS measurements. Bull. Seismol. Soc. Am. 92 (4), 1377–1389. https://doi.org/10.1785/0120000922.

Linde, A., Gladwin, M.T., Johnston, M.J.S., Gwyther, R.L., Bilham, R.G., 1996. A slow earthquake sequence on the San Andreas fault. Nature 383, 65–68. https://doi.org/10.1038/383065a0.

Lisowski, M., 2007. Analytical Volcano Deformation Source Models, in: Volcano Deformation. Springer Praxis Books, Berlin, Heidelberg, pp. 279–304.

Liu, Y., Rice, J.R., 2007. Spontaneous and triggered aseismic deformation transients in a subduction fault model. J. Geophys. Res. 112, B09404. https://doi.org/10.1029/2007jb004930.

Lo Giudice, E., Rasà, R., 1992. Very shallow earthquakes and brittle deformation in active volcanic areas: the Etnean region as an example. Tectonophysics 202, 257–268. https://doi.org/10.1016/0040-1951(92)90111-I.

Maramai, A., Graziani, L., Brizuela, B., 2021. Italian Tsunami Effects Database (ITED): the first Database of Tsunami Effects observed along the Italian coasts. Front. Earth Sci. 9, 596044 https://doi.org/10.3389/feart.2021.596044.

Montgomery-Brown, E.K., Segall, P., Miklius, A., 2009. Kilauea slow slip events: Identification, source inversions, and relation to seismicity. J. Geophys. Res. 114, B00A03. https://doi.org/10.1029/2008JB006074.

Neri, M., Acocella, V., Behncke, B., Maiolino, V., Ursino, A., Velardita, R., 2005. Contrasting triggering mechanisms of the 2001 and 2002–2003 eruptions of Mount Etna (Italy). J. Volcanol. Geotherm. Res. 144 (1–4), 235–255. https://doi.org/10.1016/j.jvolgeores.2004.11.025.

Obara, K., Hirose, H., 2006. Non-volcanic deep low-frequency tremors accompanying slow slips in the southwest Japan subduction zone. Tectonophysics 417 (1–2), 33–51. https://doi.org/10.1016/j.tecto.2005.04.013.

Palano, M., 2016. Episodic slow slip events and seaward flank motion at Mt. Etna volcano (Italy). J. Volcanol. Geotherm. Res. 324, 8–14. https://doi.org/10.1016/j.jvolgeores.2016.05.010.

Palano, M., Aloisi, M., Amore, M., Bonforte, A., Calvagna, F., Cantarero, M., Consoli, O., Guglielmino, F., Mattia, M., Puglisi, B., Puglisi, G., 2006. Kinematics and strain analyses of the eastern segment of the Pernicana fault (Mt. Etna, Italy) derived from geodetic techniques (1997–2005). Ann. Geophys. 49, 1105–1117. https://doi.org/10.4401/ag-3103.

Palano, M., Gresta, S., Puglisi, G., 2009. Time-dependent deformation of the eastern flank of Mt. Etna: after-slip or viscoelastic relaxation? Tectonophysics 473, 300–311. https://doi.org/10.1016/j.tecto.2009.02.047.

Palano, M., Rossi, M., Cannavò, F., Bruno, V., Aloisi, M., Pellegrino, D., Pulvirenti, M., Siligato, G., Mattia, M., 2010. Etn@ref: a geodetic reference frame for Mt. Etna GPS networks. Ann. Geophys. 53 (4), 49–57. https://doi.org/10.4401/ag-4879.

Palano, M., Viccaro, M., Zuccarello, F., Gresta, S., 2017. Magma transport and storage at Mt. Etna (Italy): a review of geodetic and petrological data for the 2002-03, 2004 and 2006 eruptions. J. Volcanol. Geotherm. Res. 347, 149–164. https://doi.org/10.1016/j.jvolgeores.2017.09.009.

Pareschi, M.T., Boschi, E., Mazzarini, F., Favalli, M., 2006. Large submarine landslides offshore Mt. Etna. Geophys. Res. Lett. 33 (13), L13302 https://doi.org/10.1029/2006GL026064.

Pezzo, G., Palano, M., Tolomei, C., De Gori, P., Calcaterra, S., Gambino, P., Chiarabba, C., 2020. Flank sliding: a valve and a sentinel for paroxysmal eruptions and magma ascent at Mount Etna, Italy. Geology 48 (11), 1077–1082. https://doi.org/10.1130/G47656.1.

Rasà, R., Azzaro, R., Leonardi, O., 1996. Aseismic creep on faults and flank instability at Mount Etna volcano, Sicily. Geol. Soc. Spec. Publ. 110 (1), 179–192. https://doi.org/10.1144/GSL.SP.1996.110.01.14.

Rogers, G., Dragert, H., 2003. Episodic tremor and slip on the Cascadia subduction zone: the chatter of silent slip. Science 300 (5627), 1942–1943. https://doi.org/10.1126/science.1084783.

Rubin, A.M., 2011. Designer friction laws for bimodal slow slip propagation speeds. Geochem. Geophys. Geosyst. 12, Q04007 https://doi.org/10.1029/2010gc003386.

Saastamoinen, J., 1972. Atmospheric correction for the troposphere and stratosphere in radio ranging satellites. In: The Use of Artificial Satellites for Geodesy, vol. 15, pp. 247–251. https://doi.org/10.1029/GM015p0247.

Segall, P., Rubin, A.M., Bradley, A.M., Rice, J.R., 2010. Dilatant strengthening as a mechanism for slow slip events. J. Geophys. Res. 115, B12305. https://doi.org/10.1029/2010jb007449.

Solaro, G., Acocella, V., Pepe, S., Ruch, J., Neri, M., Sansosti, E., 2010. Anatomy of an unstable volcano from InSAR: Multiple processes affecting flank instability at Mt. Etna, 1994-2008. J. Geophys. Res. 115, B10405 https://doi.org/10.1029/2009JB000820.

Spampinato, L., Sciotto, M., Cannata, A., Cannavò, F., La Spina, A., Palano, M., Salerno, G.G., Privitera, E., Caltabiano, T., 2015. Multiparametric study of the February–April 2013 paroxysmal phase of Mt. Etna New South-East crater. Geochem. Geophys. Geosyst. 16 (6), 1932–1949. https://doi.org/10.1002/2015GC005795.

Tarquini, S., Isola, I., Favalli, M., Battistini, A., 2007. TINITALY, A Digital Elevation Model of Italy with a 10 m-Cell Size (Version 1.0). Istituto Nazionale di Geofisica e Vulcanologia (INGV).

Tibaldi, A., Groppelli, G., 2002. Volcano-tectonic activity along structures of the unstable NE flank of Mt. Etna (Italy) and their possible origin. J. Volcanol. Geotherm. Res. 115, 277–302. https://doi.org/10.1016/S0377-0273(01)00305-5.

Urlaub, M., Petersen, F., Gross, F., Bonforte, A., Puglisi, G., Guglielmino, F., Krastel, S., Lange, D., Kopp, H., 2018. Gravitational collapse of Mount Etna's southeastern flank. Sci. Adv. 4 (10), eaat9700. https://doi.org/10.1126/sciadv.aat9700.

Urlaub, M., Geersen, J., Petersen, F., Gross, F., Bonforte, A., Krastel, S., Kopp, H., 2022. The submarine boundaries of Mount Etna's unstable southeastern flank. Front. Earth Sci. 10, 810790 https://doi.org/10.3389/feart.2022.810790.

Vigliotti, L., 2008. Comment on "Lost tsunami" by Maria Teresa Pareschi et al. Geophys. Res. Lett. 35 (2), L02608 https://doi.org/10.1029/2007GL031155.

Wech, A.G., Bartlow, N.M., 2014. Slip rate and tremor genesis in Cascadia. Geophys. Res. Lett. 41 (2), 392–398. https://doi.org/10.1002/2013GL058607.

Wessel, P., Luis, J.F., Uieda, L., Scharroo, R., Wobbe, F., Smith, W.H.F., Tian, D., 2019. The Generic Mapping Tools version 6. Geochem. Geophys. Geosyst. 20, 5556–5564. https://doi.org/10.1029/2019GC008515.